Study of wave-induced seabed response around twin pipelines in sandy seabed through laboratory experiments and numerical simulations

Yanyan Zhai[1,2,3], Jisheng Zhang[1,2], Yakun Guo[4], Zihao Tang[1,2], Tiantian Zhang[5]

[1] Key Laboratory of Coastal Disaster and Defence (Hohai University), Ministry of Education, China

[2] College of Harbor, Coastal and Offshore Engineering, Hohai University, Nanjing, 210098, China

[3] Department of Mechanical Engineering, Technical University of Denmark, DK-2800 Kgs. Lyngby, Denmark

[4] Faculty of Engineering & Informatics, University of Bradford, Bradford, BD7 1DP, UK

[5] China Three Gorges Corporation, Beijing, 100038, China

Corresponding email: jszhang@hhu.edu.cn, y.guo16@bradford.ac.uk

Abstract: Wave-seabed-pipelines interaction is of critical importance in the design of submarine pipelines. Previous studies mainly focus on investigating the characteristics of flow fields and hydrodynamics around a single pipeline. In this study, laboratory experiments and numerical simulations have been performed to examine the effect of burial depth and space between the centers of twin pipelines on the wave-seabed-twin pipelines interaction subject to waves. In the mathematical model, the Volume-Averaged Reynolds-Averaged Navier-Stokes (VARANS) equations are used to describe the wave motion in the fluid domain, while the seabed domain is described by using the Biot's poro-elastic theory. Numerical models are validated using these experimental measurements and available relevant experimental data. Experimental and numerical results indicate that the burial depth and relative position of twin pipelines can significantly affect the wave-averaged flow velocity field and the pore-water pressure distribution as well as effective stress.

Keywords: twin pipelines; burial depth; space between twin pipelines; pore-water pressure; effective and additional stress.

1 Introduction

In offshore engineering, submarine pipelines are usually used to transport crude oil and gas from offshore to onshore areas. Their stability in harsh offshore environmental conditions plays a crucial role in the design of pipelines. Ocean wave is the primary factor that causes the pipeline instabilities. Many offshore pipelines have been reported to be damaged by ocean waves (Christian et al., 1974; Herbich et al., 1984; Sumer and Fredsøe, 2002; Sumer, 2014). Due to its practical significance, the wave-induced submarine pipeline instability has been extensively investigated in past

decades, with a primary focus on a single pipeline by means of theoretical and experimental methods as well as numerical simulations (e.g. MacPherson 1978; Mcdougal et al. 1988; Sumer et al. 1999, 2001; Jeng and Cheng, 2000; Gao et al. 2003; Damgaard et al. 2006; Sui et al. 2016; Lin et al. 2017).

MacPherson (1978) investigated the wave-driven pore-water pressure in permeable seabed and found that the seepage force was essential. Cheng and Liu (1986) applied the boundary integral equations to investigate the wave-induced soil response. They found that in a rectangular region with impermeable walls, both the uplift seepage force and pore-water pressure around the buried pipeline were affected by wave and seabed parameters. McDougal et al. (1988) applied an analytical approach to investigate the wave generated forces acting on the buried pipeline in an infinite seabed. Around a fully buried pipeline, the effect of a cover layer on the wave-induced seabed dynamic response was examined by Jeng and Cheng (2000); Gao and Wu (2006) and Zhou et al. (2014) using the finite element method. Sumer et al. (1999, 2001) conducted laboratory experiments to investigate the stability of liquefied seabed in the vicinity of pipelines and the onset of scour underneath the pipeline subjected to currents/waves. Their studies illustrated that the excessive seepage flow and the resultant piping caused the onset of the scouring under the pipeline. The effect of upward seepage force on the scour beneath a single pipeline was also studied by Li et al. (2020a). The progressive wave-induced seabed dynamic response around a buried pipeline was further investigated by Sumer et al. (2006) with laboratory experiments. They concluded that the effect of pipeline on the pore pressure buildup at the top of the pipe was negligible. The soil liquefaction first occurred in the top shallow layer and then developed downwards. However, this situation changed around the vicinity of the pipe. Zhou et al. (2011) carried out laboratory experiments to examine the combined effect of wave and current on the soil dynamic responses around a single pipeline. Their studies revealed that the current could intensify the erosion process for all types of tested soils while the pore-water pressure within the sandy seabed slightly decreased with elapse of time. Yang et al. (2012a, b, 2014) experimentally investigated the seabed scouring process around a marine pipeline induced by waves. To protect pipe from scouring damage, they found that attaching a spoiler on its top or placing a rubber underneath the pipe was effective provided that the length of the spoiler or rubber was larger than a critical value. Recently, Sun et al. (2019) conducted laboratory experiments to examine the wave induced seabed response around a partially buried pipeline in a trenched layer. They found that the trench depth and the thickness of the buried layer had a significant effect on the pore pressure within the trench. This is also valid for twin pipelines that the trench and backfilling have a major influence on the wave-driven seabed response, but it generally exists during the pipelines construction rather than the operation phase. Some recent studies have further evaluated the liquefaction potential around a trenched pipeline in terms of transient liquefaction (Qi et al.,

2020) and residual liquefaction (Chen et al., 2019), respectively. Apart from the numerical studies, Miyamoto et al., (2020) carried out a number of wave flume tests in a drum centrifuge to investigate the wave-induced soil liquefaction around a shallowly buried pipeline. More development and studies on the pipeline-seabed interaction can be found in a state-of-the-art review by Fredsøe (2016).

Comparing with the studies on a single pipeline, limited studies have been conducted to investigate the wave-induced seabed response around twin pipelines, though pipelines may also be laid in parallel (Hirschhausen et al., 2018). In the previous studies, the twin pipelines were treated individually because the distance between them was very large in practice. With the reduction of horizontal gap, the twin pipelines become more dependent and do not behave like a single extended body (Li et al., 2020b). Therefore, more attention should be paid to the twin pipelines with a small gap. Bearman et al. (1985) investigated the in-line force on cylinders with general cross-section, which was in a condition of planar oscillatory flow with small amplitude. They compared the theoretical analysis with experimental results and evaluated the inviscid inertial force at low Keulegan-Carpenter (KC) numbers. Tatsuno (1989) performed laboratory experiments to examine the steady flow patterns around two circular cylinders at low Reynolds numbers. The effects of radii ratio, the distance in between and the flow direction on the streamline patterns were discussed. Tang et al. (2015) applied a three-step finite element method to study the effect of the center-to-center distance between the two cylinders and the gap between the lowest surface of the twin cylinders and the plane wall on the hydrodynamic force coefficients, Strouhal numbers, and vortex shedding modes. Their study demonstrated that the hydrodynamic force coefficients and vortex shedding modes differed significantly, with respect to various combinations of the center-to-center distance and the gap. They also found that the change in the vortex shedding modes could result in a pronounceable augment in the root mean square values of drag and lift coefficients. However, these studies on the twin cylinders did not consider the effect of the porous media on the flow. Cokgor and Avci (2003) conducted laboratory experiments to measure the forces on the circular cylinder, laid on or partly buried in the bed with parallel twin dummy cylinders nearby. Their study showcased that for the tandem cylinder case, the pressure value around the circular cylinder was smaller than that with a single cylinder and was closely related to the buried depth and the center-to-center distance. Cokgor and Avci (2006) further conducted laboratory experiments to investigate the flow dynamic characteristics around the parallel twin dummy cylinders under wave-current action. Their results showed that the force coefficients relatively decreased with the increase of the burial depth and the presence of the second cylinder. Furthermore, the tested cylinder also reduced the force coefficients compared with the case of a single cylinder for otherwise identical conditions. Using a mathematical model, Zhang et al. (2013) examined the impacts of buried depth

and distance between centers of twin pipelines on the hydrodynamic force and flow field distribution around twin pipelines without considering the seabed response. In their models, the sandy bed was treated as a rigid porous material. Their results revealed that an increasing distance between centers of twin pipelines led to an increase of velocity magnitude and a decrease of wave pressure around pipelines. In addition, the decrease of the buried depth resulted in the increment in velocity and size of vortex in both the front and lee side of twin pipelines, while wave pressure behind the pipelines decreased. Zhao et al. (2015) numerically studied the seabed scour around tandem pipelines under steady current and different pipeline gap conditions. The results highlighted that scour depth below the downstream pipeline was smaller than that under the upstream pipeline.

Regarding the twin pipelines, these investigations mainly examined the characteristics of flow fields and hydrodynamics without considering the pipeline gap conditions and the buried depths in a detailed manner while the gaps and the buried depths play an essential role in the resulting flow and the seabed response. This stimulates the present study in which laboratory experiments and numerical simulations are conducted to investigate the wave-induced soil response around the twin pipelines subject to wave conditions. Both the buried depths and the gap conditions are taken into account. In the experiments, the variations of pore pressure around the twin pipelines are investigated, aiming to reveal the potential instability area. The model adopted in this study has not yet been applied to study the seabed response in the presence of the twin pipelines. The model is validated using the measured data. The validated model is then performed to compute the distributions of both the pore pressure and the additional stress in the whole domain. The experiments and the numerical model complement each other and provide insight into the soil response at the circumstances of various buried depths and distances in between.

2 Experiments

To look into the practical wave-soil-twin pipelines interaction, wave flume test is an appropriate and effective approach. The different buried depths and distances between the centers of the twin pipelines can be easily realized. In this study, 32 twin pipelines cases and one single pipeline case are tested.

2.1 Experimental setup

Experiments are carried out in a 50 m long, 1.0 m wide and 1.3 m deep wave flume, at Hohai University, China. The experiments are regarded as a small prototype without adopting any scale at a 1g condition (g is the gravitational acceleration), in which the soil in a field test can be used in model experiments without particle size scaling (Hettler

2000). Figure 1 shows the laboratory experimental setup. Plywood floors on both sides of the sediment basin are constructed to elevate the bottom of the flume by 0.25 m. To ensure smooth transformation of the waves before entering the measurement section, two 1:10 slopping plywood ramps are built at the ends of the 7.5 m long false floor. The wave flume is equipped with a piston-type wave generator and two porous, slopping wave absorbers at both ends to reduce wave reflections. The wave maker generates regular waves with a period of 0.6–2.5 s and an amplitude of up to 0.2 m. Four wave-height gauges whose measurement range and precision are 0.60 m and 0.1 mm respectively, are installed along the central axis of the test section to record the wave height (see Figure 1 for gauges arrangements). The water depth at the measurement section is maintained at 0.40 m for all runs.

The sediment basin has a dimension of 2.0 m long, 1.0 m wide and 0.58 m deep, resided in the middle section of the flume. The properties of sediment used in the laboratory experiments are listed in Table 1, where γ_s and γ_w are the unit weight of soil and water, respectively. The shear modulus G is measured by the shear wave velocity method, and the tri-axial test is used to obtain the Poisson's ratio. The Young's modulus (E) is calculated based on the measured shear modulus and the Poisson's ratio. The permeability coefficient is measured by the constant head permeability test.

Table 1 Properties of the tested sediment

Parameter	Symbol	Value
Mean grain size	d_{50} (mm)	0.15
Maximum void ratio	$e_{\max}$	0.871
Minimum void ratio	$e_{\min}$	0.411
Void ratio	e	0.584
Porosity	N	0.369
Relative density	$D_r = \frac{e_{\max} - e}{e_{\max} - e_{\min}}$	0.624
Specific gravity of sediment grain	$G_s = \gamma_s / \gamma_w$	2.68
Permeability	k (m/s)	3.57×10^{-5}
Poisson's ratio	ν	0.30
Effective confining pressure	σ_0' (Kpa)	1.35
Elasticity modulus	$E = 2G(1+\nu)$ (MN/m^2)	53.82
Shear modulus	G (MPa)	8.28

To form the sandy bed, sands and water are mixed thoroughly using an ordinary mixer that can release the air from the sand into thick slurry in a large plastic box. The thick slurry is then slowly pumped into the sand tank by a suction pumper and is allowed to consolidate for several hours. This process is repeated to ensure that the mudline reaches the

top rim of the sand tank. Water is then slowly pumped into the flume to reach the designated water depth (h = 0.4 m). Static hydraulic pressure of still water is imposed on the sandy seabed for 72 hrs to ensure the seabed subsidence is negligible. This means that the variation of the void ratio is dismissed and the artificial factors will not affect the saturation degree of the sandy bed. Two PMMA (poly-methyl-methacrylate) pipes are used in the experimental runs to model natural pipelines. For all experimental runs, the length and the external diameter are 1.0 m and 12 cm, respectively (D_m = D_r = 12 cm, where D_m and D_r are the diameters of the twin pipelines). Eight pore-pressure transducers are evenly installed around the circumference of the measurement pipeline at the center section (see Figure 1). These pore-pressure sensors are produced by Chengdu Smart World Technology Co., Ltd with the measurement range and full scale accuracy being 30 kPa and ± 0.1% respectively. The center of twin pipelines is placed at the same buried depth (D_m/4, 0.5D_m, 3D_m/4 and D_m respectively), and the distance (L) between the centers of twin pipelines varies from 1.5D_m to 3D_m, with an interval of 0.5D_m. The pore-water pressures in the seabed and wave heights are measured simultaneously in all tests with the same sampling frequency of 50 Hz. Both sides of twin pipelines are fixed on telescopic rods installed on a non-removable shelf. The shelf ensures that the pipelines are unmovable horizontally and vertically. However, the telescopic rods make sure the pipelines could move in the vertical direction. The vertical pipes movement occurs mainly in the pre-consolidation process, and it is negligible small during the measurements, thereby not being analyzed.

2.2 Experimental conditions and procedures

The experimental conditions of wave, sandy seabed and pipelines in this study are chosen based on the previous laboratory experiments (Zhai et al. 2018, Sun et al. 2019, Zhao et al. 2018) and listed in Table 2, in which H = wave height and T = wave period. Only two wave periods (T = 1.2 and 1.4 s) and one water depth (d = 0.4 m) are analyzed since the wave period and water depth is not the focus of the present work. The duration of data collection in all tests is 180 s. Wave condition falls in the Stokes' third-order zone with the diagram of 'the range of suitability of various wave theories' proposed by Lé Mehauté (1976), as shown in Figure 2 (Sumer and Fredsøe, 1999; Lé Mehauté, 1976; Tzang, 1992).

The tests are conducted for four burial depths and four distances between the centers of the twin pipelines for the given wave condition. The experimental procedures are as follows:

(1) Eight small holes are drilled in the pipeline for installing the pore-pressure transducers and are sealed with waterproof tape. To locate the measured pore-water pressures on the pipeline surface, the surface of the transducers

is flushed. The transducers, equipped with sand filters, are installed in water for 24 hrs aiming to drive out all air. The measured hydrostatic pressure is an indicator for the examination of air condition in the transducers. The measured data, in agreement with the theoretical value, are regarded as having no air existence in the transducers.

(2) The test soils are mixed with water and pumped into the soil basin. The twin pipelines are then placed at the planned positions in the sand tank. Finally, a scraper is used to trim the seabed.

(3) The flume is then slowly filled with water to the prescribed water level and the soil is left to consolidate for three days.

(4) Switch on the wave generator and record the water surface elevation and the pore pressure simultaneously.

(5) Switch off the wave generator and empty the water in the flume.

(6) The sand pit is emptied after completing an experimental run and then steps (2)–(5) are repeated until all the planned experimental runs are completed.

Table 2 Experimental conditions

Case	Wave condition		Relative buried depth d_t/D_m	Distance between the centers of twin pipelines L/D_m
	Wave height H (cm)	Wave period T (s)		
1	10	1.2	1/4	1.5
2	10	1.2	1/2	1.5
3	10	1.2	3/4	1.5
4	10	1.2	1	1.5
5	10	1.2	1/4	2
6	10	1.2	1/2	2
7	10	1.2	3/4	2
8	10	1.2	1	2
9	10	1.2	1/4	2.5
10	10	1.2	1/2	2.5
11	10	1.2	3/4	2.5
12	10	1.2	1	2.5
13	10	1.2	1	3
14	10	1.2	1/4	3
15	10	1.2	1/2	3
16	10	1.2	3/4	3
17	10	1.4	1/4	1.5
18	10	1.4	1/2	1.5
19	10	1.4	3/4	1.5
20	10	1.4	1	1.5
21	10	1.4	1/4	2
22	10	1.4	1/2	2

23	10	1.4	3/4	2
24	10	1.4	1	2
25	10	1.4	1/4	2.5
26	10	1.4	1/2	2.5
27	10	1.4	3/4	2.5
28	10	1.4	1	2.5
29	10	1.4	1	3
30	10	1.4	1/4	3
31	10	1.4	1/2	3
32	10	1.4	3/4	3
33	10	12	1	-

3. Numerical simulations

3.1 Numerical model

In this paper, the WSSI model proposed by Zhang et al. (2011) is used to simulate the complex wave-seabed-pipelines interaction, in which the porous seabed deformation is assumed to be very small and has no effect on wave transformation above seabed. The wave model COBRAS (Lin and Liu, 1999), based on the volume-averaged Reynolds-averaged Navier-Stokes (VARANS) equations, is applied to calculate the wave pressure and effective stress on the solid-liquid interface. The output of the flow velocity and the wave pressure along seabed surface from the wave model are imposed as boundary conditions at the seabed surface in the seabed model. In the WSSI model, Lin and Liu (1999) developed an internal wave-maker for wave generation. The concerned section is far away from the damping zones. Figure 3 presents the numerical model setup, which is the same dimension as in the experiment. The numerical model is chosen because of its good performance in simulating the wave-seabed-breakwater interaction (Zhang et al., 2011). However, the applicability of the model to pipelines needs to be validated, which is discussed in Section 4.2. Both the pore pressure and the additional stress in the whole domain are simulated using the model to investigate the influence of the distance between pipelines and the buried depth on the seabed response.

3.1.1 Wave model

Many researchers have studied the wave motion and seepage flow in the porous structures by solving the VARANS equations (Shao, 2010; Hsu, Sakakiyama, and Liu, 2002). The mass and momentum conservation equations are:

$$\frac{\partial \langle \bar{u}_{fi} \rangle}{\partial x_i} = 0 \tag{1}$$

$$\frac{\partial\langle\bar{u}_{fi}\rangle}{\partial t}+\frac{\langle\bar{u}_{fj}\rangle}{n(1+c_A)}\frac{\partial\langle\bar{u}_{fi}\rangle}{\partial x_j}=\frac{1}{1+c_A}\left[-\frac{n}{\rho_f}\frac{\partial\langle\bar{p}_f\rangle}{\partial x_i}-\frac{\langle\overline{\partial u'_{fi}u'_{fj}}\rangle}{\partial x_j}+\frac{1}{\rho_f}\frac{\langle\bar{\tau}_{ij}\rangle}{\partial x_j}+ng_i\right]$$
$$-\frac{\langle\bar{u}_i\rangle}{1+c_A}\left[\frac{a(1-n)^2}{n^2d_{50}^2}+\frac{b(1-n)}{n^2d_{50}}\sqrt{\langle\bar{u}_{f1}\rangle^2+\langle\bar{u}_{f2}\rangle^2}\right] \quad (2)$$

where $\langle\bar{u}_{fi}\rangle$ = the Reynold-averaged flow velocity, x_i = the Cartesian coordinate, ρ_f = water density, $\langle\bar{p}_f\rangle$= the Reynold-averaged water pressure, $\bar{\tau}_{ij}$= the Reynold-averaged viscous stress tensor of the mean flow, g_i = the gravity acceleration, d_{50} = the equivalent mean diameter of the porous material, c_A = the added mass coefficient, *a* and *b* = empirical coefficients associated with the linear and nonlinear drag forces, respectively. The effect of turbulence fluctuation on the mean flow, denoted as $\langle u'_{fi}u'_{fj}\rangle$, is obtained by solving the modified *k*-*ε* turbulence model, where *k* = the kinetic energy and *ε* = the dissipation rate of the kinetic energy (Lin and Liu, 1998). The prime denotes turbulence fluctuation regarding the ensemble mean. The Darcy's volume averaging operator '〈 〉' is defined as

$$\langle a\rangle=\frac{1}{V}\int_{V_f}adv, \quad (3)$$

where V = the total averaging volume, and V_f = the portion of V occupied by fluid.

The finite-difference method (FDM) is used to solve the wave model COBRAS. To decouple the VARANS equations, two-step projection method is adopted. Highly precise solution in space is achieved by using the high-order finite difference scheme of staggered grid. A modified VOF method is applied to track the free surface of wave. The interfacial force between fluid and solids is obtained in accordance with the extended Forchheimer equation. In the momentum equations, both the linear and nonlinear drag forces between the pore water and the soil skeleton are included.

3.1.2 Seabed model

In the WSSI model, a seabed model based on the Biot's poro-elastic theory/equation (Biot, 1941) is applied to investigate pore pressure, soil displacement and effective stress of the seabed consisting of uniform and isotropic porous medium. Though dynamic analysis is useful to understand the variation of the pore-water pressure in saturated seabed, it is much complex than the quasi-static analysis method (Simon et al. 1986; Grabe et al. 2014). Previous studies also showed that the quasi-static analysis of porous media, ignoring the acceleration of solid particles and pore fluid, is able to simulate the dynamic response of saturated porous media (Sumer 2014). In this study, the static Biot consolidation equation in conjunction with the linear isotropic elastic model is applied to appropriately model the

wave-induced dynamic response of the sandy seabed, which has small deformation and no residual pore pressure accumulation.

The Biot's equation is:

$$\nabla^2 p_p - \frac{\gamma_w n\beta}{k}\frac{\partial p_p}{\partial t} = \frac{\gamma_w}{k}\frac{\partial}{\partial t}\left(\frac{\partial u_s}{\partial x} + \frac{\partial w_s}{\partial y}\right), \quad (4)$$

where p_p = wave-induced oscillatory pore pressure; k = the permeability in different directions taken as the same value in all directions; n = the seabed soil porosity; u_s and w_s = the soil displacements in the x- and y-directions, respectively, and β = the compressibility of pore fluid given by (Veruijt, 1969):

$$\beta = \frac{1}{K_f} + \frac{1-S_r}{p_{w0}}, \quad (5)$$

where K_f = the true modulus of elasticity of pure water (2×10^9 N/m^2), p_{w0} = the absolute water pressure (1.013×10^5 N/m^2), and S_r = the degree of soil saturation (Yamamoto et al., 1978).

The force equilibrium equations are obtained based on the conservation of momentum:

$$\frac{\partial \sigma'_{xx}}{\partial x} + \frac{\partial \tau_{xy}}{\partial y} = \frac{\partial p_p}{\partial x}, \quad (6)$$

$$\frac{\partial \tau_{xy}}{\partial x} + \frac{\partial \sigma'_{yy}}{\partial y} = \frac{\partial p_p}{\partial y}, \quad (7)$$

where σ'_{xx} and σ'_{yy} = the effective normal stresses in the horizontal and vertical directions, respectively, and τ_{xy} = the shear stress in xy plane.

Based on the generalized Hooke's law, the relationships between effective stresses and soil displacements are derived as:

$$\sigma'_{xx} = 2G\left[\frac{\partial u_s}{\partial x} + \frac{\mu_s}{1-2\mu_s}\left(\frac{\partial u_s}{\partial x} + \frac{\partial w_s}{\partial y}\right)\right], \quad (8)$$

$$\sigma'_{yy} = 2G\left[\frac{\partial w_s}{\partial y} + \frac{\mu_s}{1-2\mu_s}\left(\frac{\partial u_s}{\partial x} + \frac{\partial w_s}{\partial y}\right)\right], \quad (9)$$

$$\tau_{xy} = G\left[\frac{\partial w_s}{\partial x} + \frac{\partial u_s}{\partial y}\right], \quad (10)$$

where G = shear modulus is computed by Young's modulus (E) and Poisson's ratio (μ_s) in the form of $E/(2(1+\ \mu_s))$.

3.2 Boundary and initial conditions

To solve the VARANS equations, appropriate boundary and initial conditions must be specified. No-slip boundary condition is used on the seabed surface, where the kinetic energy k and kinetic energy dissipation rate $\varepsilon = 0$. On the

free surface, the atmospheric pressure, the normal stress, tangential stress, the gradient of k and ε are all equal to zero. In order to avoid wave reflection at two ends, weakly reflecting boundary condition and numerical sponge layers are adopted.

For evaluation of wave-induced seabed response, both the vertical effective normal stress and shear stress at the surface of the permeable seabed are assumed to be zero. On the seabed surface, the pore-water pressure is assumed to be the same as the dynamic wave pressure (p_b) obtained from the wave model:

$$p_p = p_b,\ \sigma'_{yy} = 0,\ \tau_{xy} = 0 \ \text{ at } y = h_s, \tag{11}$$

The bottom of the seabed is assumed as an impermeable rigid bottom without soil movements and vertical flow:

$$\frac{\partial p_p}{\partial y} = 0,\ u_s = 0,\ w_s = 0 \ \text{ at } y = 0, \tag{12}$$

Assume two lateral boundaries of seabed be impermeable without horizontal soil displacement and flow motion (Zhou et al. 2014):

$$\frac{\partial p_p}{\partial x} = 0,\ u_s = 0 \ \text{ at } x = x_b \ \text{ and } x = x_e, \tag{13}$$

where x_b and x_e = the horizontal coordinates at the start and end of the sand tank, respectively. The boundary condition for the surface of the twin pipelines is specified as a rigid impermeable material and no fluid flows through the pipeline surface.

4 Results

4.1 Measured pore-water pressure around twin pipelines

In general, dynamic pore pressure exhibits variations in the process of wave propagation. To illustrate this, Figure 4 shows, at eight pipeline surface positions (P1–P8), the measured time-series of wave-induced excess pore-water pressure ($\Delta u = p_b - p_p$). The residual pore-water pressure is negligibly small in a sandy seabed for all experimental tests, which is also reported in Jeng and Seymour (2007) and Jeng (2018). This is mainly ascribed to the fact that the grain size of sediment used in this study is too large (d_{50} = 0.15 mm) to generate the residual pore-water pressure. The Δu induced by the wave loading is fully dissipated before the next wave arrives. It is apparent that, in the vicinity of the tested pipe, the Δu decreases towards the seabed bottom. Figure 4 also displays that the Δu in the stoss side of the tested pipeline is larger than that in its lee side.

To analyze the effect of the buried depth on the soil response, the variation of the excess pore pressure amplitude ($|\Delta u|$), at the distance L/D_m = 2, is selected for illustration. Figure 5 plots the $|\Delta u|/p_0$ profiles with respect to the d_t/D_m at three test points (P4–P6), in which p_0 is the amplitude of dynamic wave pressure at the mud-line surface, calculated by the linear wave theory. Figure 5 shows that, for T =1.2 and 1.4 s, variations of $|\Delta u|/p_0$ with d_t/D_m are similar, but the $|\Delta u|/p_0$ value at T =1.4 s is slightly greater than that at T =1.2 s for all three points. As expected, the $|\Delta u|/p_0$ decreases with the increase of the embedment depth. The maximum $|\Delta u|/p_0$ value occurs at P6 and the minimum value appears at P5, the pressure gradient between the two test points decreases with the increasing d_t/D_m. Figure 5 also illustrates that the $|\Delta u|/p_0$ attenuates greater in the smaller buried depth than that in the larger buried depth, which is primarily attributed to the effect of permeability and deformation properties of the soil. This phenomenon differs from the law of monotonous decay of the pore pressure as the augment of the seabed depth without any pipeline (Zhang et al., 2016).

Similar to the buried depth, the distance between pipelines also affects the excess pore pressure variations. Figure 6 presents, at d_t/D_m = 0.5, the $|\Delta u|/p_0$ changes with regards to L/D_m at five locations (P3–P7) for T =1.2 and 1.4 s. The $|\Delta u|/p_0$ at different points decreases as the L/D_m increases from 1.5 to 3.0. For almost all points around the measured pipeline, the attenuation rate of $|\Delta u|/p_0$ is about 10%. This is mainly ascribed to the blocking effect induced by another pipeline on the soil deformation, which decreases gradually with the increase of L/D_m. Besides, the $|\Delta u|/p_0$ attenuation from P3 to P4 is faster than that from P4 to P5; and from P7 to P6 the change is also greater than that from P6 to P5. These observations are consistent with the results of Sun et al., (2019), in which one partially buried pipeline is considered. They found larger amplitude attenuation of excess pore-water pressure occurs in the upper layer of the seabed and the smaller amplitude attenuation appears in the lower layer.

4.2 Comparison of measured and simulated results

To validate the numerical model, comparisons are made in terms of the wave elevation (η) and Δu with the same wave period, as shown in Figure 7. Figure 7(a) compares the measured and simulated η at the same point away from the right end of the wave generation zone. In addition, water elevation obtained from the analytical solution by Stokes (1880) is also plotted in Figure 7(a) for comparison. The simulated wave profile agrees well with both the measurements and the analytical results. At P3, Figure 7(b) presents the simulated and measured Δu with d_t/D_m = 1 and L/D_m = 2. Overall, the simulated pore pressure is in good agreement with the measurements, demonstrating that the present model is capable of accurately simulating the wave induced seabed response around twin pipelines.

To further validate the model, the simulated $|\Delta u|$ around twin pipelines and single pipeline is compared with the corresponding experimental results. Figure 8 presents the distributions of $|\Delta u|$ with $d_t = D_m = D_r = 12$ cm. It suggests that $|\Delta u|$ decreases in the vicinity of both the twin and single pipelines with the increase of the seabed depth; the pore pressure is larger at the pipeline top and smaller at the bottom. These are in line with the findings of Pan and Wang (2007), who considered a fully buried single pipeline in a sandy seabed. In particular, for the twin pipelines, $|\Delta u|$ at the top is more than twice the one at the bottom, which is consistent with the pressure distribution of a single pipeline. It is apparent that, for both cases, the numerical results agree well with the experimental data, which further validates the numerical model. Figure 8 also presents that the $|\Delta u|$ around the measured twin pipelines is larger than that in the vicinity of the single pipeline. A possible explanation for this result is that the seepage path of pore water is dispersed by the existence of the other pipeline; and the seepage scattering affects the propagation approach of pore pressure energy transferred from wave-induced seafloor pressure. The energy propagates into the seabed via soil particles directly (Tisato and Quintal, 2014) or spreads along the pipeline to its bottom and subsequently downward to the seabed bottom.

4.3 Comparison between twin and single pipelines

To examine the effect of the pipeline on the wave induced time-dependent seabed response, the simulated time series of Δu and stresses (effective stress and shear stress) at the bottom for the twin and the single pipeline are plotted in Figure 9. The effective stress is a summation of the additional stress induced by the wave and initial stress under self-weight consolidation state. It shows that Δu value at the bottom of the twin pipelines is larger than that of the single one; the maximum Δu value is about 0.054 kPa for the former and it is approximately 0.034 kPa for the latter. This demonstrates that the existence of the downstream pipeline has a significant effect on the pore pressure of the immediate upstream one. On the contrary, the stresses at the bottom are smaller than those for the single pipeline. It presents that the maximum value of the horizontal effective stress σ'_{xx} for the former is about 0.008 kPa, while the value of the latter is 0.012 kPa. The maximum values of the vertical effective stress σ'_{yy} for twin and single pipelines are 0.015 and 0.021 kPa, respectively. At the bottom, the Δu value for the twin pipeline is almost twice that for the single. The opposite is the case for effective stress. This illustrates that the twin pipelines are more prone to instability than the single pipeline. However, the presence of the downstream pipeline has an insignificant effect on the shear stress τ_{xy} at the bottom of the upstream pipeline. This is evidenced in Figure 9(d) that the τ_{xy} at the twin pipelines bottom is about 0.062 kPa, which is slightly smaller than that for the single one (0.069 kPa). This reveals that, around

the upstream pipeline, the downstream one mainly affects the effective stresses and pore pressure, while its effect on the shear stress is relatively weak. This is because the fact that the excess pore pressure, transmitted through soil particles and pore water attenuates the periphery of pipelines, definitely dominates the stress.

To visualize the variation of the seabed responses in the whole field, Figure 10 displays the distributions of Δu and the additional stress in the seabed, with H = 10 cm, T = 1.2 s, $d_t = D_m = 12$ cm and $L = 2D_m$. The selected moment is the wave trough passing the single pipe and the upstream pipeline of twin pipes. It shows a similar variation of Δu along the seabed depth, namely the Δu in the upper layer of the seabed decays faster than that in the lower layers, which is primarily due to the change in soil permeability and deformation properties. Compared to the single pipeline, the distribution for both Δu and additional stresses around the twin pipes is not the same. That is, the circumferential asymmetric distribution of Δu and additional stress is negligible for single pipeline, while the asymmetric distribution is profound for twin pipes. The difference is especially significant regarding the vertical additional stress (σ_y') induced by the wave. At the downstream of the upstream pipeline, it is noted that the area with large σ_y' values shrinks compared with that of single pipeline. Moreover, the distributions of shear stress τ_{xy} are similar for both the single and the twin cases. It indicates that the effect of the downstream pipeline on the tangential stress around the upstream pipeline is negligible.

5. Discussions

To evaluate the seabed instability in the presence of twin pipelines, the effects of the buried depth and the distance in between on the wave-induced dynamic response, in terms of flow patterns, pore pressure and additional stresses are discussed in this section. In the following figures, the x' and y' are the local coordinates as also marked in Figure 3: x' is placed on the seabed surface (positive in streamwise direction); y' is perpendicular to x' and passes through the pipeline centerpoint (positive towards the free surface).

5.1 Effect of the buried depth

The seabed response is directly induced by the flow variations. Wave-induced flow field around twin pipelines is different from that around a single pipeline, as illustrated by Lin et al. (2016). Therefore, the variation of flow fields in the vicinity of the twin pipelines is analyzed first. Figure 11 shows the flow patterns around the twin pipelines at four moments (t_1-t_4), in which, the seabed surface is at y = 0.57 m, $L = 2D_m$. A vortex in the proximity of the upstream pipeline is well developed at t_2 and t_4, corresponding to the wave crest and wave trough passing by, respectively. In

contrast, a vortex is generated in the vicinity of the downstream pipeline at t_1 and t_3. According to Mao (1987), the vortex formed in the two sides of the downstream pipeline is one of the main factors transporting sediment away from the foundation, resulting in the onset of scour around pipeline. The vortex, formed at the lee side of the downstream pipeline, transports more sediment away from the pipeline and has a larger threat to the stability of twin pipelines.

At different embedment depths (d_t/D_m = 0, 0.25, 0.5, 0.75 and 1.0), Figure 12 illustrates the velocity fields around the twin pipelines. Between the two pipelines, the flow exhibits similar patterns with respect to the varied d_t/D_m; the velocity magnitude is much smaller on the whole but it becomes larger as d_t/D_m increases. The decrease of velocity magnitude also results in an increase of wave pressure, which is reported by Zhang et al. (2013). An appreciable vortex occurs in the front of the downstream pipeline. With the increase of d_t/D_m, the vortex shifts downwards and its size gradually becomes smaller, and it disappears completely when d_t/D_m= 1. The existence of vortex results in the seabed scouring in the proximity of the pipelines. As d_t/D_m increases, the vortex becomes weaker and the seabed stability is enhanced. This implies that the scour usually occurs around partially embedded pipelines, and the scour scope is the largest for thoroughly exposed pipelines (e.g. $d_t/D_m = 0$).

Regarding the partially buried pipelines in the sandy seabed, it may also undergo sinking or floatation due to wave-induced liquefaction (Sumer et al., 1999; Teh et al., 2003, 2006). Therefore, evaluation of the excess pore-water pressure and the stability of the soil layer below the pipeline is of great engineering importance. Two positions in the vicinity of the upstream pipeline, i.e., x = 20 m, y = 0.43 m and x = 20.07 m, y = 0.50 m are selected for illustration. Figure 13 shows the simulated $|\Delta u|/p_0$ profiles versus time for different d_t/D_m. Figure 13(a) demonstrates that, immediately under the upstream pipeline, $|\Delta u|/p_0$ significantly decreases as d_t/D_m increases, and Figure 13(b) reveals that d_t/D_m has a marginal effect on $|\Delta u|/p_0$. The comparison of Figures 13(a) and (b) indicates that the effect of embedment depth on excess pore pressure at the bottom is more significant than that at the lee side. That is mainly ascribed to the sheltering effect of the pipeline on the pore pressure propagating from upstream to downstream. Meanwhile, the seepage path at the bottom of the pipeline is considerably different from that in the lee side of the pipeline. As aforementioned, wave-induced pressure propagates into seabed via two ways, either transmitting along the pipelines surface, or passing through the sediment particles. In shallow buried depth, where the friction effect of particles is comparatively small, the pore pressure delivered by the two ways is almost the same. However, with the augment of d_t/D_m, the friction effect becomes significant; the excess pore pressure transferred through particles decays intensely and thereby the pressure transmission through the circumference of the pipeline dominates the stress

field.

Figure 14 shows the horizontal and vertical distributions of the maximum excess pore pressure Δu_{max} at the circumstance of various embedment depths. In Figure 14(a), Δu_{max} profile in the vicinity of the pipelines is generally symmetric. This illustrates that the larger d_t/D_m results in the smaller Δu_{max} in the horizontal direction. As d_t/D_m increases from 0.25 to 1.0, the attenuation of Δu_{max} at x'/D_m = -1, 0 and 1 is 5.6%, 8.8% and 7.9%, respectively. This means that as d_t/D_m increases, the attenuation of Δu_{max} at the bottom of two pipelines is larger than that in the distance in between and the stoss side of the upstream pipeline. In addition, the influence of d_t/D_m on $\Delta u_{\max}$ declines as x'/D_m ascends from -2 to 0 and from 2 to 4. This is because the embedment depth affects not only the velocity amplitude, the position and size of the vortex, but also the seepage path of pore water around pipelines. The rapid growth of velocity amplitude at the top of the pipeline (see Figure 12) demonstrates the reason that the pore pressure underneath the pipeline is the smallest in the seabed around the vicinity of pipeline. Figure 14(b) presents the distribution of Δu_{max} along the vertical direction at x = 20.07 m with various d_t/D_m. It demonstrates that, with the increasing d_t/D_m, Δu_{max} decreases along the depth. As discussed by Neelamani and Al-Banaa (2012), further augment in burial depth results in a reduction of horizontal and vertical components of the wave force acting on the pipeline, leading to the attenuation of the excess pore-water pressure around the pipelines. Moreover, this can be also ascribed to the friction effect between pore water and soil particles within the pore seabed.

Also at the two positions: x = 20 m, y = 0.43 m and x = 20.07 m, y = 0.50 m, Figure 15 presents the variation of the wave-induced additional stresses for different embedment depths. Figure 15(a) shows that the additional stress under the upstream pipeline increases with the decrease of d_t/D_m. The maximum amplitude of σ_y' drops noticeably with the increment of $\frac{d_t}{D_m}$. For example, the values of σ_y' for $d_t =$ 0.5, 0.75 and 1.0D_m is only about 84%, 45% and 15% of that for d_t = 0.25D_m. Meanwhile, a time lag is also observed between $d_t = D_m$ and other three cases (e.g. $d_t =$ 0.25, 0.5 and 0.75D_m) with respect to the occurrence of the maximum additional stress. For instance, comparing with $d_t = 0.25D_m$, the time lags with $d_t = D_m$ in the vertical and the horizontal directions are 0.6 s and 0.2 s, respectively. σ_y' at x = 20.07 m, y = 0.50 m also illustrates a similar phenomenon for amplitude attenuation, as shown in Figure 15(b), but the time lag is negligible with the decreasing d_t/D_m. The transient additional stress attenuates sharply as d_t/D_m increases to 1.0. σ_y', as one part of σ_{yy}', is an essential proxy and σ_y' can be used to analyze the instability of the seabed, based on Okusa, (1985)'s instantaneous liquefaction criterion. It is indicated that with the reduction of

d_t/D_m, the seabed in the vicinity of pipelines is more vulnerable to liquefaction damage, as shown in Figure 15. This signifies that compared with partially buried pipelines, the fully buried ones are more insulated from the threat of instability due to the seabed liquefaction. These results are consistent with previous results reported by Palmer (2008) and Sun et al., (2019) that studied a single pipeline laid in an open trench with various backfilled depths.

Figure 16 demonstrates the effect of the embedment depths on the maximum additional stresses along horizontal direction y = 0.43 m and vertical direction x = 20.07 m. Figure 16(a) shows that the maximum vertical additional stress $(\sigma_y')_{max}$ around the pipelines declines as d_t/D_m increases from 0.25 to 1.0. The $(\sigma_y')_{max}$ between the two pipelines is larger than that in their both sides for d_t = 0.25, 0.5 and 0.75D_m; however, as the pipelines are fully buried ($d_t = D_m$), the $(\sigma_y')_{max}$ in the two places is almost the same. The $(\sigma_y')_{max}$ in the vicinity of the twin pipelines is smaller than that farther away from the pipelines. These results reveal that, in the relatively shallow buried depth, e.g., $d_t =$ 0.25, 0.5 and 0.75 D_m, the seabed near the twin pipelines is the most likely to occur liquefaction. On the contrary, for $d_t = D_m$, the seabed closing to the twin pipes is the most stable position. The maximum horizontal additional stress $(\sigma_x')_{max}$ under the pipelines decreases with the increase of d_t/D_m. In the twin pipes downstream, $(\sigma_x')_{max}$ is smaller than that upstream, which is because the seepage path is interrupted due to the existence of the pipelines. Figure 16(b) illustrates that $(\sigma_y')_{max}$ in the vertical direction decreases with the increment of d_t/D_m. This implies that the smaller the d_t/D_m is, the easier the seabed instability occurs. The position of the peak $(\sigma_x')_{max}$ in the vertical direction moves downwards as d_t/D_m augments. For example, at $y'/h_s =$ -0.5, increasing d_t/D_m from 0.25 to 1.0 with an interval of 0.25, $(\sigma_y')_{max}$ is reduced by 8.4%, 10.4% and 32.6%, respectively, indicating that the attenuation of the vertical additional stress augments with the increasing buried depth. The variation of $(\sigma_x')_{max}$ in the vertical direction between d_t = 0.75 and 1.0 D_m is more pronounceable than that between d_t = 0.25 and 0.5D_m. In the lower soil layer, $(\sigma_x')_{max}$ drops as d_t/D_m increases, and that the effect of d_t/D_m on $(\sigma_x')_{max}$ is more profound in the upper soil layer than that in the lower layer.

Based on the analyses of flow patterns, excess pore pressure and additional stresses around the vicinity of the twin pipelines, it can be concluded that large buried depth could prevent the pipelines from seabed instability induced by liquefaction, and the buried depth at $d_t = D_m$ is believed to satisfy the requirement for the pipeline stability.

5.2 Effect of the distance between the twin pipelines

Figure 17 shows the effect of the different distances between pipelines (L/D_m) on the flow patterns for d_t/D_m = 0.5.

It is seen from Figure 17 that there are no separate vortices between the pipelines when the L/D_m = 1.5 (Figure 17(a)). This illustrates that the two pipelines are significantly dependent on each other. As L/D_m increases to 2, two separate vortices occur in the lee side of the upstream pipeline and the stoss side of the downstream pipeline, respectively. As L/D_m further increases from 2 to 3, the vortices remain attached to the pipelines and no vortex shedding occurs. This may be ascribed to the fact that the relatively small spacing between the pipelines partially inhibits the vortex shedding. The vortex size gradually grows and the scour potential becomes greater. Furthermore, as the augment of L/D_m, the velocity magnitude above the downstream pipeline increases significantly, while the magnitude above the upstream has an insignificant variation. Between the two pipelines, the velocity magnitude experiences decrease with the increasing L/D_m, leading to the increase in wave pressure. As a result, the wave induced excess pore pressure increases.

To further analyze the seabed response around the pipelines, the variations of the normalized maximum excess pore pressure $(\Delta u)_{max}/p_0$ along horizontal direction y = 0.50 m and vertical direction x = 20.07 m are plotted in Figure 18. For given distances between pipelines ($e.g. L$ = 1.5, 2.0, 2.5 and 3.0 D_m), $(\Delta u)_{max}/p_0$ profiles along y = 0.5 m display similar changes. At the bottom of the pipelines, $(\Delta u)_{max}/p_0$ reaches the smallest, as shown in Figure 18(a). Figure 18 also illustrates that with the decreasing L/D_m, $(\Delta u)_{max}/p_0$ under the pipelines increases first and then declines, and that on both sides of the upstream pipeline exhibits a similar variation. The reason is that the influence of the distance on the seepage path and the velocity magnitude around the vicinity of the upstream pipeline diminishes non-monotonously when the distance between two pipelines increases. However, $(\Delta u)_{max}/p_0$ between the two pipelines increments monotonously with the increase of L/D_m, which is mainly caused by the decrease of velocity magnitude. This phenomenon is consistent with the result shown in Figure 17. The variation of $(\Delta u)_{max}/p_0$ between the two pipelines is more noticeable than that in their surroundings. On the lee side of both pipelines, $(\Delta u)_{max}/p_0$ reaches the maximal at L/D_m = 2.5, while it reaches the minimal when L/D_m = 1.5. In Figure 18(b), for a certain L/D_m, $(\Delta u)_{max}/p_0$ along x = 20.07 m presents a declining trend as the seabed depth increases. $(\Delta u)_{max}/p_0$ in the upper part of the seabed attenuates faster than that in the lower part, which is mainly attributed to the changes in soil permeability and deformation properties. It also demonstrates that $(\Delta u)_{max}/p_0$ with L/D_m = 1.5 in the upper soil layer is slightly smaller than that with other L/D_m values ($e.g. L/D_m$ = 2.0, 2.5 and 3.0). The variation of $(\Delta u)_{max}/p_0$ is negligible as L/D_m increases from 2.0 to 3.0. To summarize, the twin pipelines distance mainly affects the pore pressure distribution in between and at the upper seabed layer.

The relative position of pipelines affects the distributions of additional stress around the pipelines, as shown in Figure

19. Figure 19(a) presents that, under the upstream pipeline, $(\sigma_y')_{max}/p_0$ reaches the maximum and minimum as L/D_m = 1.5 and 2.0, respectively. The minimum value of $(\sigma_y')_{max}/p_0$ between the pipelines decreases with the increase of L/D_m. This means that the seabed instability between the pipelines becomes higher as L/D_m decreases. $(\sigma_y')_{max}/p_0$ attenuates by 30%, 25% and 20% as L/D_m increases from 1.5 to 3.0 with an interval of 0.5, respectively. The effect of distance on $(\sigma_x')_{max}/p_0$ under the upstream pipeline is negligible, and $(\sigma_x')_{max}/p_0$ on both sides of the downstream pipeline augments as L/D_m increases from 1.5 to 3.0. Figure 19(b) shows that, along x = 20.07 m, the additional stress profiles with different L/D_m are similar. $(\sigma_y')_{max}/p_0$ for L/D_m =1.5 is larger than that for other L/D_m values ($e.g. L/D_m$ = 2.0, 2.5 and 3.0). $(\sigma_x')_{max}/p_0$ decreases gradually with the increasing L/D_m as y' = 0–0.07 h_s. However, $(\sigma_x')_{max}/p_0$ has an opposite variation trend when y' = 0.07–0.26 h_s. As y' > 0.26 h_s, $(\sigma_x')_{max}/p_0$ profiles with different L/D_m almost coincide. The impact of distance between pipelines on the horizontal additional stress is not apparent, especially in the lower part of the seabed. To conclude, as the distance between twin pipelines increases, the two pipelines become more independent. As a result, separate pore pressure and additional stress profiles are formed around the two pipelines. According to the attenuation trend of additional stress, it is speculated that the twin pipelines can be treated as two single ones when L/D_m > 4.

6 Conclusions

In this study, comprehensive experimental and numerical investigations on soil dynamic responses around twin pipelines, subjected to waves in the sandy seabed, are carried out for a range of embedment depths and distances between pipeline centers. The main conclusions are:

(1) Pore-water pressure decreases towards the seabed bottom around the vicinity of the tested pipe. The pressure on the left half of the upstream pipeline is larger than that on its right side. Pore pressures around the twin pipelines are larger than those around the vicinity of the single pipeline for otherwise identical conditions. The simulated pore pressure agrees well with the measurements.

(2) The downstream pipeline mainly affects effective stress and pore pressure around the upstream pipeline, while the effect of the downstream pipeline on the shear stress around the upstream pipeline is negligible.

(3) The seabed stability around the proximity of the pipelines is enhanced when d_t/D_m increases. The effect of embedment depth on velocity fields in the gap between the pipelines is insignificant. The embedment depth has a larger impact on excess pore pressure between the two pipelines than that in the stoss side of the upstream pipeline. The vertical subsidiary stress decreases with the augment of the depth. As such, the seabed instability increases as

the embedment depth becomes smaller. The buried depth of d_t/D_m = 1 is sufficient to prevent the pipelines failure from the liquefaction induced instability.

(4) Wave-induced seabed dynamics in the lee side of the upstream pipeline weakens as the distance between the centers of twin pipelines (L/D_m) increases. The velocity in the gap between twin pipelines reaches the smallest. The maximum excess pore pressure with L/D_m= 1.5 in the upper soil layer is smaller than that with other L/D_m values. The maximum vertical additional stress decreases gradually with the increase of L/D_m. Therefore, the potential instability of twin pipelines is stepped up as the gap between twin pipelines decreases. The impact of distance between twin pipelines on the horizontal additional stress is insignificant. At L/D_m = 3, the upstream and downstream pipelines tend to have similar vortex, pore pressure and vertical additional stress distributions. When L/D_m > 4, the twin pipelines can be considered as two separated single pipelines.

Acknowledgements

The authors are grateful for sponsorship from the Fundamental Research Funds for the Central Universities of China (No. 2019B61914), the Postgraduate Research & Practice Innovation Program of Jiangsu Province, China (No. SJKY19_0527), the National Key Research and Development Program of China (2017YFC1404200), and the Marine Renewable Energy Research Project of State Oceanic Administration (GHME2015GC01). Comments made by Reviewers have significantly improved the quality of the final paper.

References

Bearman, P.W., Downie, M.J., Graham, J.M.R., Obassaju, E.D., 1985. Forces on cylinders in viscous oscillatory flow at low KeuleganCarpenter numbers. Journal of Fluid Mechanics 154, 337–356.

Biot, M.A., 1941. General theory of three- dimensional consolidation. Journal of Applied Physics 12, 155–164.

Chen, R., Wu, L., Zhu, B., Kong, D., 2019. Numerical modelling of pipe-soil interaction for marine pipelines in sandy seabed subjected to wave loadings. Applied Ocean Research 88, 233–245.

Cheng, A.H., Liu, P.L., 1986. Seepage force on a pipeline buried in a poroelastic seabed under wave loadings. Applied Ocean Research 8, 22–32.

Christian, J.T., Taylor, P.K., Yen, J.K.C., Erali, D.R., 1974. Large diameter underwater pipeline for nuclear power plant designed against soil liquefaction. Offshore Technology Conference 597, 597–602.

Cokgor, S., Avci, I., 2003. Forces on partly buried, tandem twin cylinders in waves at low Keulegan-Carpenter numbers. Ocean Engineering 30(12), 1453–1466.

555 Cokgor, S., Avci, I., 2006. Hydrodynamic forces on partly buried, tandem twin pipelines in coexisting flow. Journal of
556 Coastal Research 39, 1783–1788.
557 Fredsøe, J., 2016. Pipeline-Seabed Interaction. Journal of Waterway, Port, Coastal and Ocean Engineering, ASCE
558 142(6), 03116002.
559 Gao, F.P., Han, X.T., Cao, J., Sha, Y., Cui, J.S., 2012. Submarine pipeline lateral instability on a sloping sandy seabed.
560 Ocean Engineering. 50, 44–52.
561 Gao, F.P., Wu, Y.X., 2006. Non-Linear Wave Induced Transient Response of Soil Around A Trenched Pipeline. Ocean
562 Engineering 33, 311–330.
563 Grabe, J., Hamann, T., Chmelnizkij, A., 2014. Numerical Simulation of Wave Propagation in Fully Saturated Soil
564 Modeled as a Two-Phase Medium. In Proceedings of the 9th International Conference on Structural Dynamics,
565 EURODYN, 631–637.
566 Herbich, J.B., Schiller, R.E., Dunlap, W.A., Watanabe, R.K., 1984. Seafloor scour-design guidelines for ocean-
567 founded structures. Marcel Dekker Inc. New York.
568 Hettler, A., 2000. Gründungskörper mit zyklischer Belastung in Sand und 1g-Modelltechnik. Bautechnik 77(12), 901–
569 908.
570 Hsu, T.J., Sakakiyama, T., Liu, P.L.-F., 2002. A numerical model for wave motions and turbulence flows in front of a
571 composite breakwater. Coastal Engineering, 46(1), 25–50.
572 Jeng, D.S., Cheng, L., 2000. Wave-induced seabed instability around a buried pipeline in a poro-elastic seabed. Ocean
573 Engineering 27, 127–146.
574 Jeng, D.-S., 2018. Mechanics of Wave-seabed-structure Interactions: Modelling, Processes and Application.
575 Cambridge University Press, Cambridge.
576 Jeng, D.-S., Seymour, B.R., 2007. Simplified analytical approximation for pore-water pressure buildup in marine
577 sediments. J. Waterway Port Coast. Ocean Eng. ASCE 133 (4), 309–312.
578 Lé Mehauté, B., 1976. An introduction to hydrodynamics and water waves. Heidelberg, Berlin: Springer 315.
579 Li, Y., Ong, M. C., Fuhrman, D. R., 2020a. CFD investigations of scour beneath a submarine pipeline with the effect
580 of upward seepage. Coastal Engineering, 156, 103624.
581 Li, Y., Ong, M. C., Fuhrman, D. R., Larsen, B. E., 2020b. Numerical investigation of wave-plus-current induced scour
582 beneath two submarine pipelines in tandem. Coastal Engineering, 156, 103619.
583 Lin, P.Z., Liu, P.L.F., 1998. A numerical study of breaking waves in the surf zone. Journal of Fluid Mechanics, 359(1),
584 239–264.

585 Lin, P., Liu, P.L.F., 1999. Internal wave-maker for Navier-Stokes equations models. Journal of Waterway, Port,
586 Coastal, and Ocean Engineering, ASCE 125(4), 207–215.
587 Lin, Z.B., Guo, Y.K., Jeng, D.S., Liao, C.C., Rey, N., 2016. An integrated numerical model for wave–soil–pipeline
588 interactions. Coastal Engineering 108, 25–35.
589 Lin, Z., Pokrajac, D., Guo, Y.K., Jeng, D.-S., Tang, T., Rey, N., Zheng, J.H., Zhang, J.S., 2017. Investigation of
590 nonlinear wave-induced seabed response around mono-pile foundation. Coastal Engineering, 121,197–211
591 MacPherson, H., 1978. Wave forces on pipelines buried in permeable seabed. Journal of Waterway, Port, Coastal and
592 Ocean Division, ASCE 104(4), 407–419.
593 Mao, Y., 1987. The interaction between a pipeline and an erodible bed. Series Paper Technical University of Denmark.
594 Miyamoto, J., Sassa, S., Tsurugasaki, K., Sumida, H., 2020. Wave-Induced Liquefaction and Floatation of a Pipeline
595 in a Drum Centrifuge. Journal of Waterway Port Coastal and Ocean Engineering-ASCE, 146(2), 04019039.
596 Neelamani, S., Al-Banaa, K., 2012. Wave force variation due to burial of submarine pipelines in uniformly graded and
597 low hydraulic conductivity soil. Applied Ocean Research 35, 47–55.
598 Okusa S., 1985. Wave-induced stress in unsaturated submarine sediments. Geotechnique, 35(4), 517–532.
599 Palmer A.C., 2008. Subsea pipeline engineering. PennWell, Oklahoma.
600 Pan D.Z., Wang L.Z., Pan C.H., Hu J.C., 2007. Experimental investigation on the wave-induced pore pressure around
601 shallowly embedded pipelines. Acta Oceanol Sin, 26(5), 125–135.
602 Qi, W., Shi, Y., Gao, F., 2020. Uplift soil resistance to a shallowly-buried pipeline in the sandy seabed under waves:
603 Poro-elastoplastic modeling. Applied Ocean Research 95, 102024.
604 Simon, B. R., Wu, J.S.-S., Zienkiewicz, O.C., Paul, D. K., 1986. Evaluation of u-w and u-<pi> finite element methods
605 for the dynamic response of saturated porous media using one‐dimensional models. International Journal for
606 Numerical and analytical methods in Geomechanics 10(5), 461–482.
607 Shao, S., 2010. Incompressible SPH flow model for wave interactions with porous media. Coastal Engineering, 57(3),
608 304–316.
609 Shi, Y. M., Wang, N., Gao, F. P., Qi, W. G., Wang, J.Q., 2019. Physical modeling of the axial pipe-soil interaction for
610 pipeline walking on a sloping sandy seabed. Ocean Engineering. 178, 20–30.
611 Stokes, G.G., 1880. On the theory of oscillation wave. Mathematical and press, 225–228.
612 Sui, T.T., Zhang, C., Guo, Y.K., Zheng, J.H., Jeng, D.S., Zhang, J.S., and Zhang, W. 2016. Three-dimensional
613 numerical model for wave-induced seabed response around mono-pile. Ships and Offshore Structures, 11(6), 667–678.
614 Sumer, B.M., 2014. Liquefaction around Marine Structures. World Scientific, New Jersey.

615 Sumer, B.M., Fredsøe, J., 2002. The Mechanics of Scour in the Marine Environment. World Scientific Publishing Co
616 Pte Ltd.
617 Sumer, B.M., Fredsøe, J., Christensen, S., Lind, M.T., 1999. Sinking/floatation of pipelines and other objects in
618 liquefied soil under waves. Coast Engineering 38, 53–90.
619 Sumer, B.M., Truelsen, C., Fredsøe, J., 2006. Liquefaction around pipelines under waves. Waterway, Port, Coastal,
620 and Ocean Engineering, ASCE 132(4), 266–275.
621 Sumer, B.M., Truelsen, C., Sichmann, T., Fredsøe, J., 2001. Onset of scour below pipelines and self-burial. Coast
622 Engineering 42, 313–335.
623 Sun, K., Zhang, J., Gao, Y., Jeng, D. S., Guo, Y., Liang, Z., 2019. Laboratory experimental study of ocean waves
624 propagating over a partially buried pipeline in a trench layer. Ocean Engineering, 173, 617–627.
625 Tang, G.Q., Chen, C.Q., Zhao, M., Lu, L., 2015. Numerical simulation of flow past twin near-wall circular cylinders
626 in tandem arrangement at low Reynolds number. Water Science and Engineering 8(4), 315–325.
627 Tatsuno, M., 1989. Steady flows around two cylinders at low Reynolds numbers. Fluid Dynamics. Res 5, 49–60.
628 Teh, T., Palmer, A., Damgaard, J.S., 2003. Experimental study of marine pipelines on unstable and liquefied seabed.
629 Coast Eng. 50 (1–2), 1–17.
630 Teh, T., Palmer, A., Bolton, M., Damgaard, J.S., 2006. Stability of submarine pipelines on liquefied seabeds. J.
631 Waterway Port Coast. Ocean Eng. ASCE 132 (4), 244–251.
632 Tisato, N., Quintal, B., 2014. Laboratory measurements of seismic attenuation in sandstone: strain versus fluid
633 saturation effects. Geophysics 79, WB9–WB14.
634 Tzang, S.Y., 1992. Water wave-induced soil fluidization in a cohesionless fine-grained seabed. PhD Thesis, University
635 of California—Berkeley, Berkeley, CA.
636 Veruijt, A., 1969. Elastic storage of aquifer, In: Flow Through Porous Media, edited by De Wiest, R. J. M., Academic
637 Press, New York, 331–376.
638 Yamamoto, T., Koning, H.L., Sellmeijer, H., van Hijum, E., 1978. On the response of a poro-elastic bed to water
639 waves. Journal of Fluid Mechanics 87 (2), 193–206.
640 Yang, L.P., Guo, Y.K., Shi, B., Kuang, C.P., Xu, W.L., Cao, S.Y., 2012(a). Study of scour around submarine pipeline
641 with a rubber plate or rigid spoiler in wave conditions. Journal of Waterways, Port, Coast and Ocean Engineering,
642 ASCE 138, 484–490.
643 Yang, L.P., Shi, B., Guo, Y.K., Wen, X.Y., 2012(b). Calculation and experiment on scour depth for submarine pipeline
644 with a spoiler. Ocean Engineering 55, 191–198.

Yang, L.P., Shi, B., Guo, Y.K., Zhang, L.X., Zhang, J.S., Han, Y., 2014. Scour protection of submarine pipelines using rubber plates underneath the pipes. Ocean Engineering 84, 176–182.

Zhai, Y., He, R., Zhao, J., Zhang, J., Jeng, D. S., Li, L., 2018. Physical model of wave-induced seabed response around trenched pipeline in sandy seabed. Applied Ocean Research, 75, 37–52.

Zhang, J.S., Jeng, D.S., Liu, P.L.F., 2011. Numerical study for waves propagating over a porous seabed around a submerged permeable breakwater: PORO-WSSI II model. Ocean Engineering 38(7), 954–966.

Zhang, J.S., Li, Q.Z., Ding, C., Zheng, J.H., & Zhang, T.T., 2016. Experimental investigation of wave-driven pore-water pressure and wave attenuation in a sandy seabed. Advances in Mechanical Engineering, 8(6), 1–10.

Zhang, J.S., Zheng, J.H., Zhang, C., Jeng, D.S., Guo, Y.K., 2013. Numerical study on the interaction between waves and twin pipelines in sandy seabed. Journal of Coastal Research 65, 428–433.

Zhao, J., Zhang, J., Dai, D., Wei, X., 2018. Experimental Investigation of Wave-Induced Pore Pressure Response Around Twin Pipelines in Seabed. In The 28th International Ocean and Polar Engineering Conference. International Society of Offshore and Polar Engineers.

Zhao, M., Vaidya, S., Zhang, Q., Cheng, L., 2015. Local scour around two pipelines in tandem in steady current. Coastal Engineering, 98, 1–15.

Zhou, C., Li, G., Dong, P., Shi, J., Xu. J., 2011. An experimental study of seabed responses around a marine pipeline under wave and current conditions. Ocean Engineering 38, 226–234.

Zhou, X., Wang, J., Zhang, J., Jeng, D.S., 2014. Wave and current induced seabed response around a submarine pipeline in an anisotropic seabed. Ocean Engineering 75, 112–127.

Figure captions

Figure 1 Sketch of the experimental set-up in the wave flume.

Figure 2 Range of suitability of various wave theories and comparison of wave condition between this study and similar experiments of Tzang (1992) and Sumer et al. (1999).

Figure 3 Sketch of the numerical model.

Figure 4 Measured pore-water pressure time series around the upstream pipeline with $d_t = D_m,\ L = 2D_m$.

Figure 5 Variation of measured excess pore pressure amplitude with different buried depths at different points: (a) T = 1.2 s and (b) T = 1.4 s (H = 10 cm, $L = 2D_m$, $D_m = D_r$ = 14 cm).

Figure 6 Variation of measured excess pore pressure amplitude with different distance between the twin pipelines at different points: (a) T = 1.2 s and (b) T = 1.4 s (H = 10 cm, $d_t = 0.5D_m$, $D_m = D_r$ = 14 cm).

Figure 7 Comparison of simulated and measured results for $d_t = D_m,\ L = 2D_m$: (a) water elevation and (b) excess pore-water pressure of P3.

Figure 8 Comparison of the experimental and numerical pore-pressure amplitudes around the upstream pipe and the single pipeline (H = 10 cm, T = 1.2 s, $d_t = D_m,\ L = 2D_m$).

Figure 9 Numerically simulated pore pressure and effective stress at the position P5 for both the twin and single pipeline(s) (H = 10 cm, T = 1.2 s, $d_t = D_m,\ L = 2D_m$).

Figure 10 Distribution of excess pore pressure and effective stress in the vicinity of twin pipelines and a single pipeline with wave trough passing the upstream pipeline with numerical model (H = 10 cm, T = 1.2 s, $d_t = D_m$ = 12 cm, $L = 2D_m$).

Figure 11 Simulated velocity field in the proximity of twin pipelines at different times over one wave period (H = 10 cm, T = 1.4 s, $L = 2D_m,\ D_m = D_r$ = 14 cm).

Figure 12 Simulated velocity field around twin pipelines for different embedment depths at time t_1 (H = 10 cm, T = 1.4 s, $L = 2D_m,\ D_m = D_r$ = 14 cm).

Figure 13 The numerical excess pore pressure time series with four buried depths at two points: (a) x = 20 m, y = 0.43 m and (b) x = 20.07 m, y = 0.50 m (H = 10 cm, T = 1.4 s, $L = 2D_m,\ D_m = D_r$ = 14 cm)

Figure 14 Distribution of the maximum excess pore pressure with different buried depths in the horizontal and vertical directions: (a) y = 0.43 m and (b) x = 20.07 m (H = 10 cm, T = 1.4 s, $L = 2D_m,\ D_m = D_r$ = 14 cm).

Figure 15 Variation of additional stress with time for different buried depths at two points (a) x = 20 m, y = 0.43 m and (b) x = 20.07 m, y = 0.50 m (H = 10 cm, T = 1.4 s, $L = 2D_m,\ D_m = D_r$ = 14 cm).

Figure 16 Distribution of the maximum additional stress with different buried depths along (a) y = 0.43 m and (b) x =

694 20.07 m (H = 10 cm, T = 1.4 s, $L = 2D_m$, $D_m = D_r$ = 14 cm).

695 Figure 17 Velocity field around twin pipelines for different values of L/D_m at time t_1 (H = 10 cm, T = 1.4 s, $d_t =$

696 $0.5D_m$, $D_m = D_r$ = 14 cm).

697 Figure 18 Distribution of the maximum excess pore pressure with different values of L/D_m along (a) y = 0.50 m and

698 (b) x = 20.07 m (H = 10 cm, T = 1.4 s, $d_t = 0.5D_m$, $D_m = D_r$ = 14 cm).

699 Figure 19 Distribution of the maximum additional stress with different values of L/D_m along (a) y = 0.50 m and (b) x

700 = 20.07 m (H = 10 cm, T = 1.4 s, $d_t = 0.5D_m$, $D_m = D_r$ = 14 cm).

701

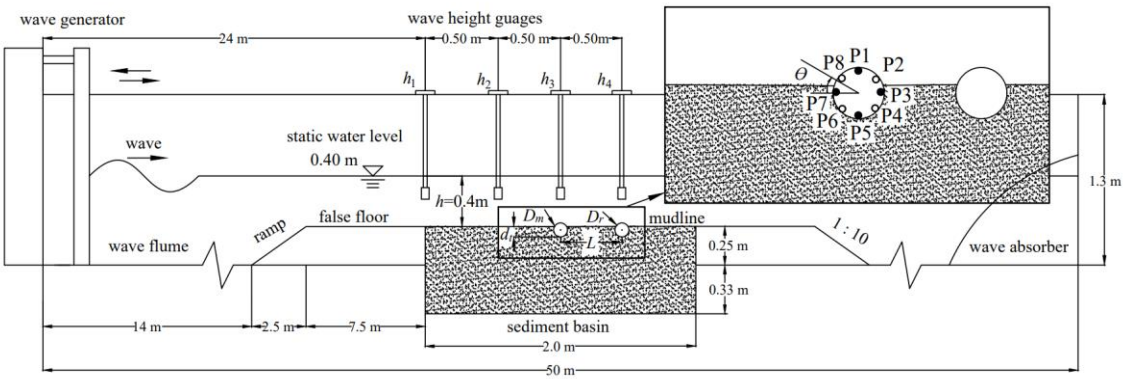

702

703 **Fig 1**

704

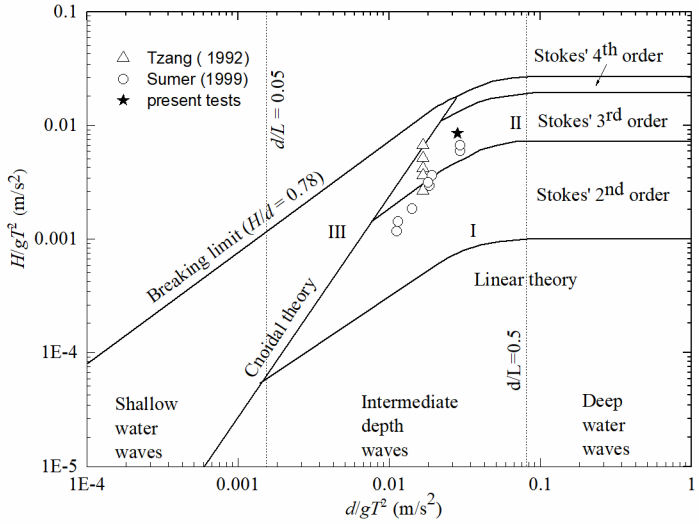

705

706 **Fig 2**

707

708

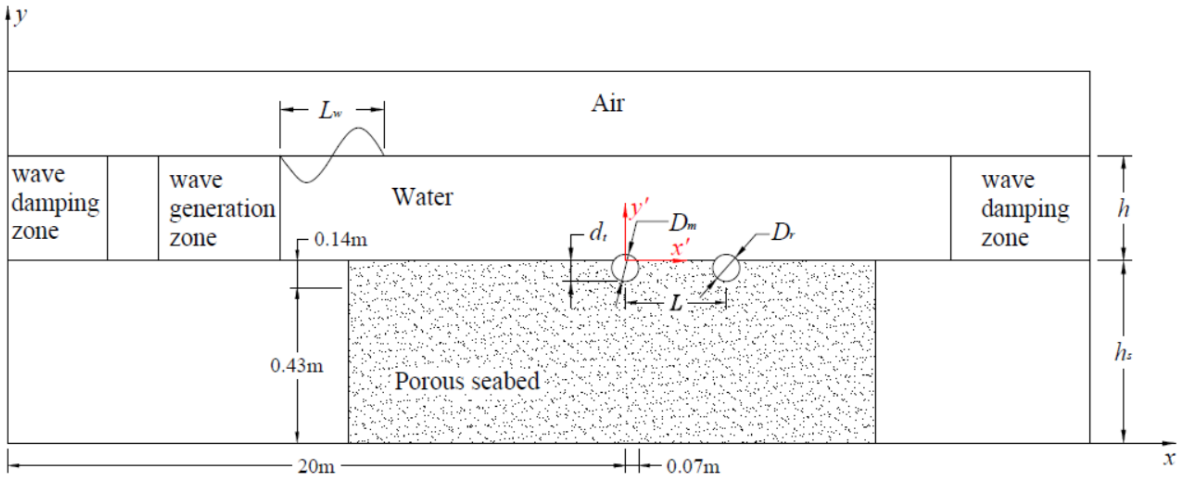

709

710

711 **Fig 3**

712

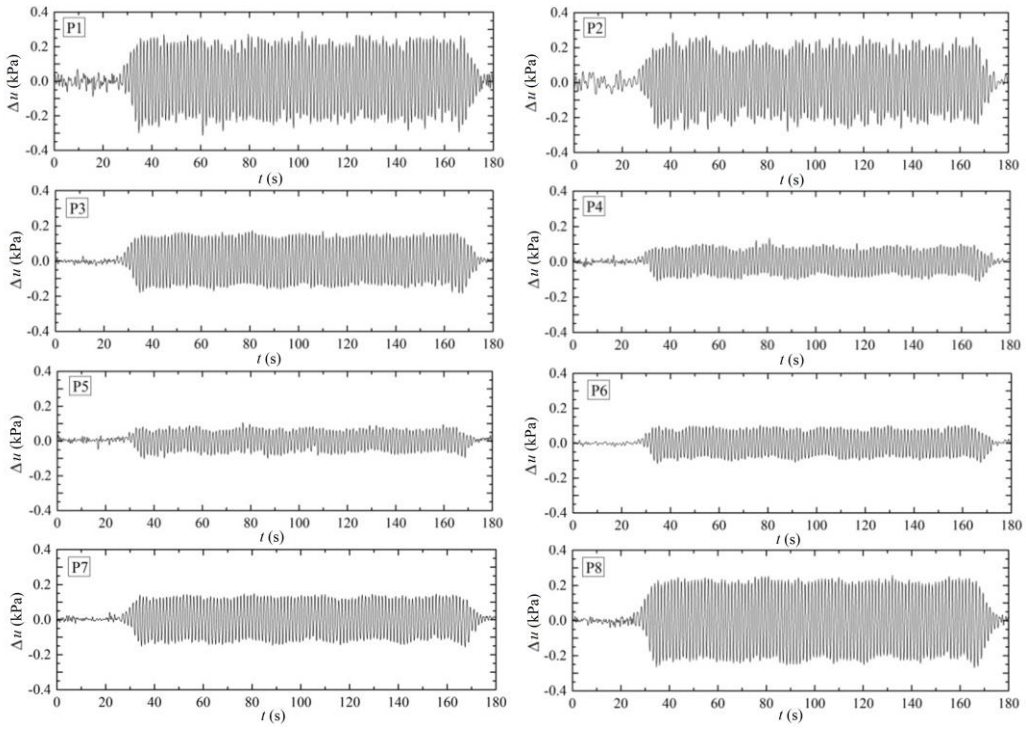

713

714

715 **Fig 4**

716

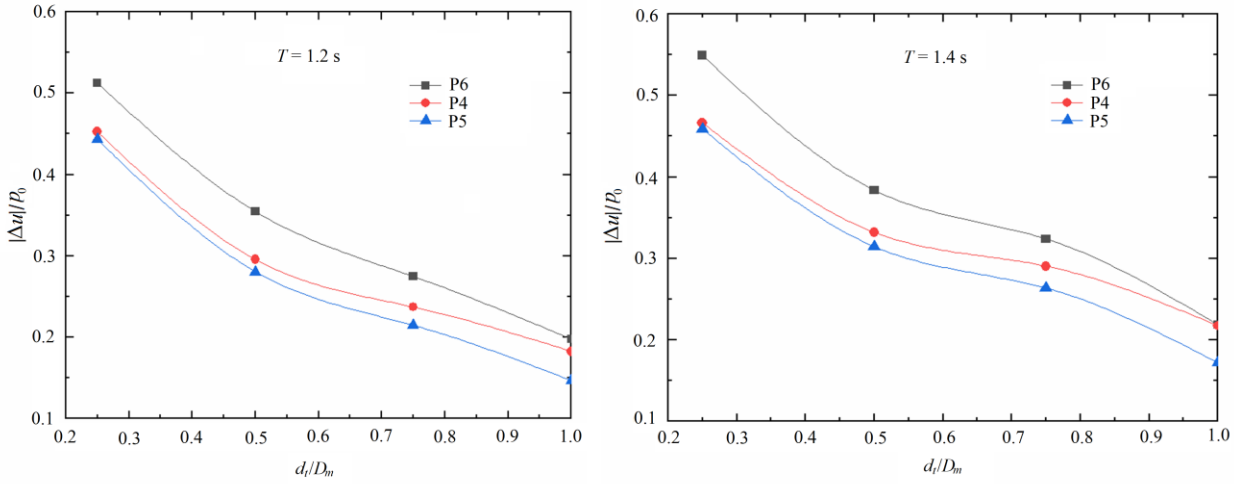

717

718 **Fig 5**

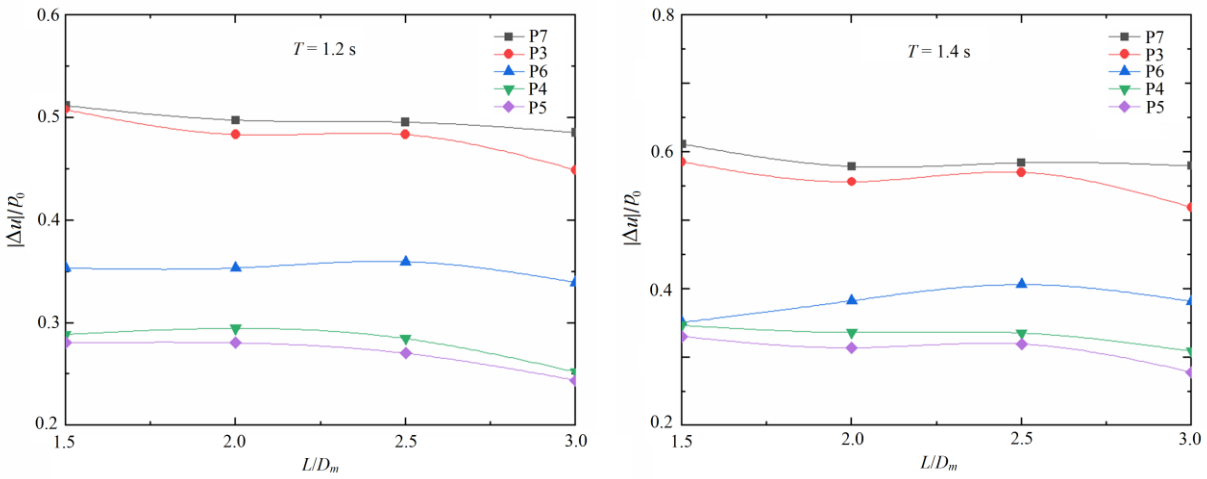

719

720 **Fig 6**

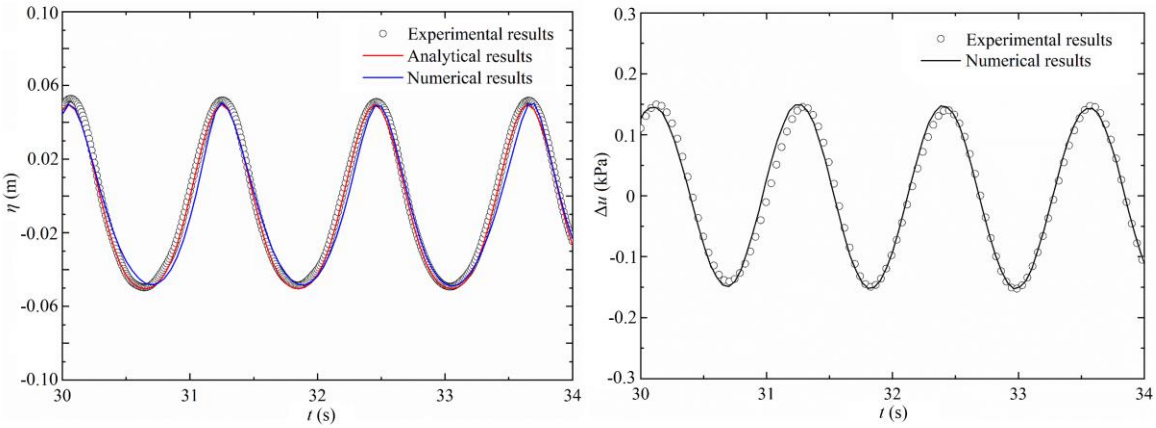

(a) water elevation (b) excess pore-water pressure measured at P3

721

722

723 **Fig 7**

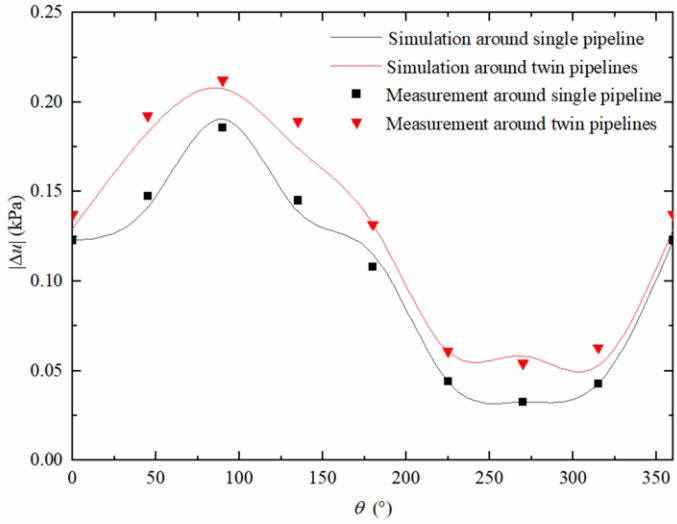

724

725 **Fig 8**

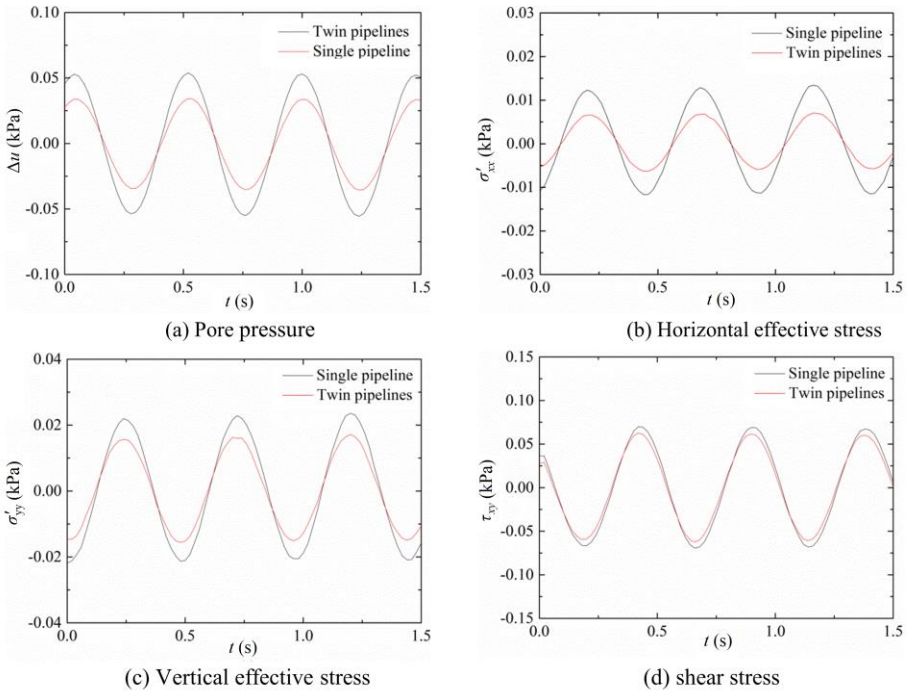

726

727 **Fig 9**

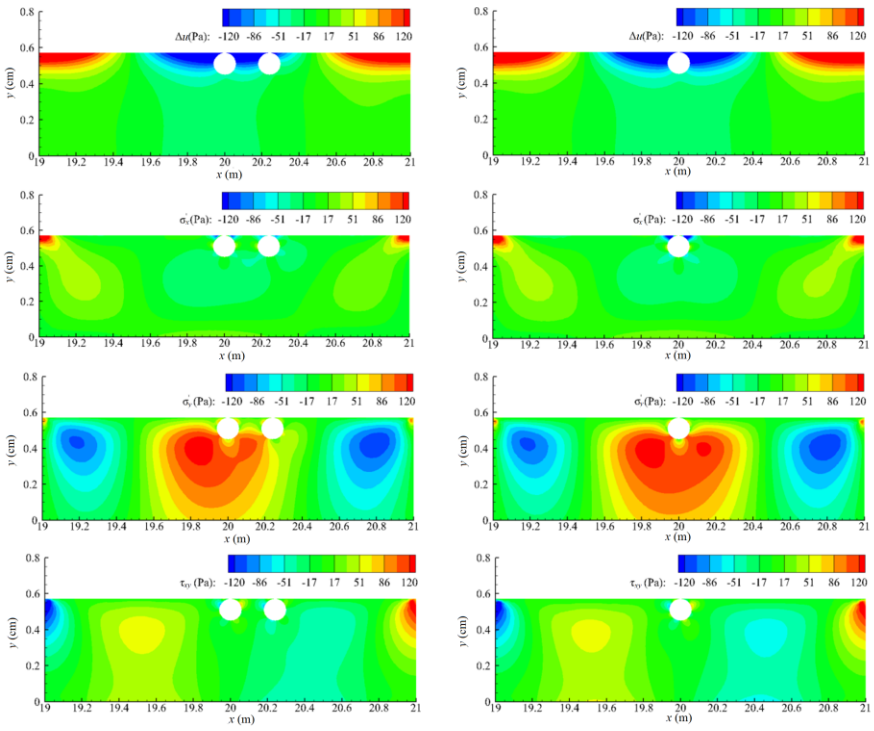

728

729 **Fig 10**

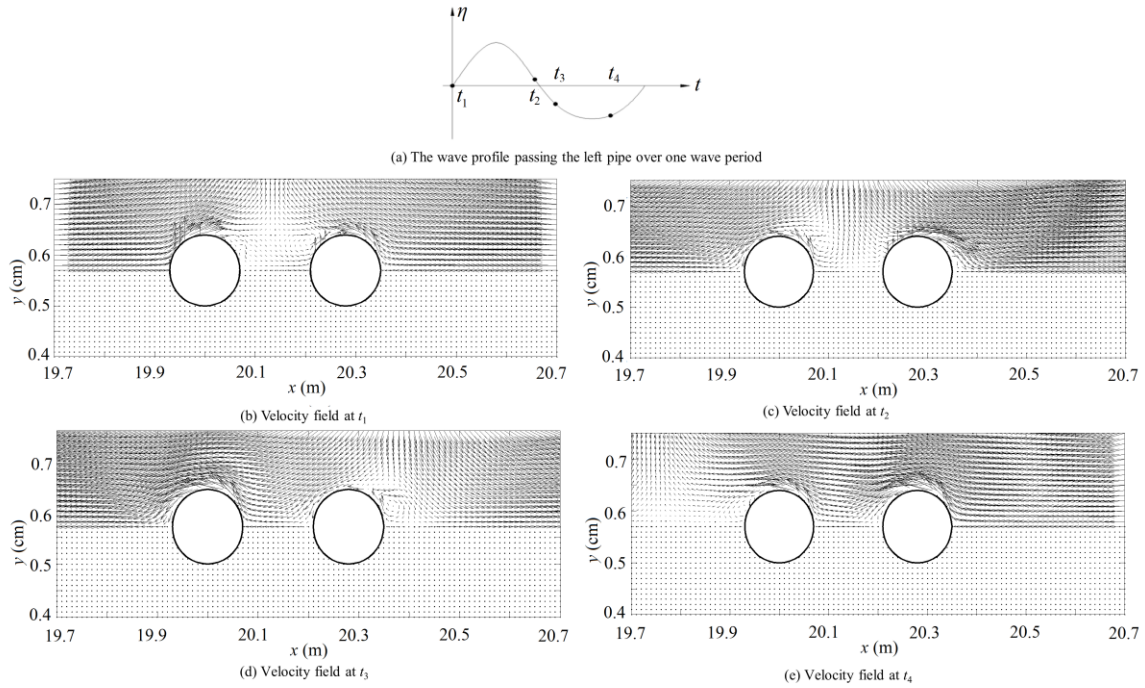

(a) The wave profile passing the left pipe over one wave period

(b) Velocity field at t_1

(c) Velocity field at t_2

(d) Velocity field at t_3

(e) Velocity field at t_4

730

731 **Fig 11**

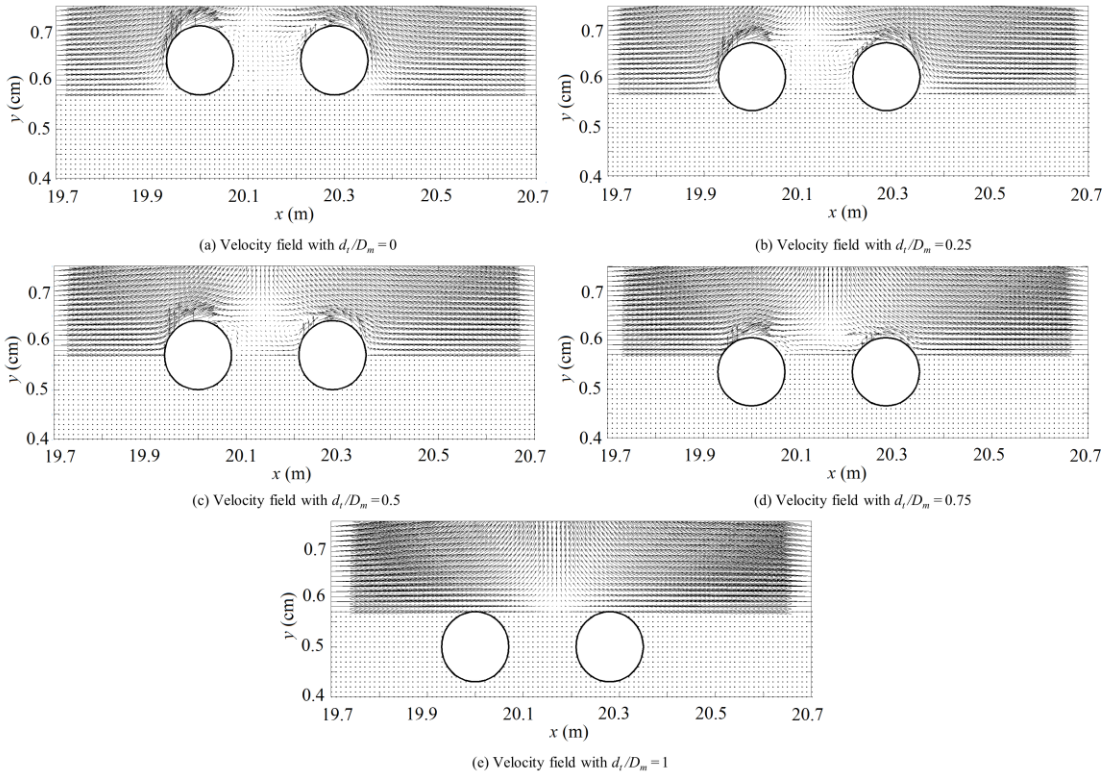

(a) Velocity field with $d_t/D_m = 0$

(b) Velocity field with $d_t/D_m = 0.25$

(c) Velocity field with $d_t/D_m = 0.5$

(d) Velocity field with $d_t/D_m = 0.75$

(e) Velocity field with $d_t/D_m = 1$

732

733 **Fig 12**

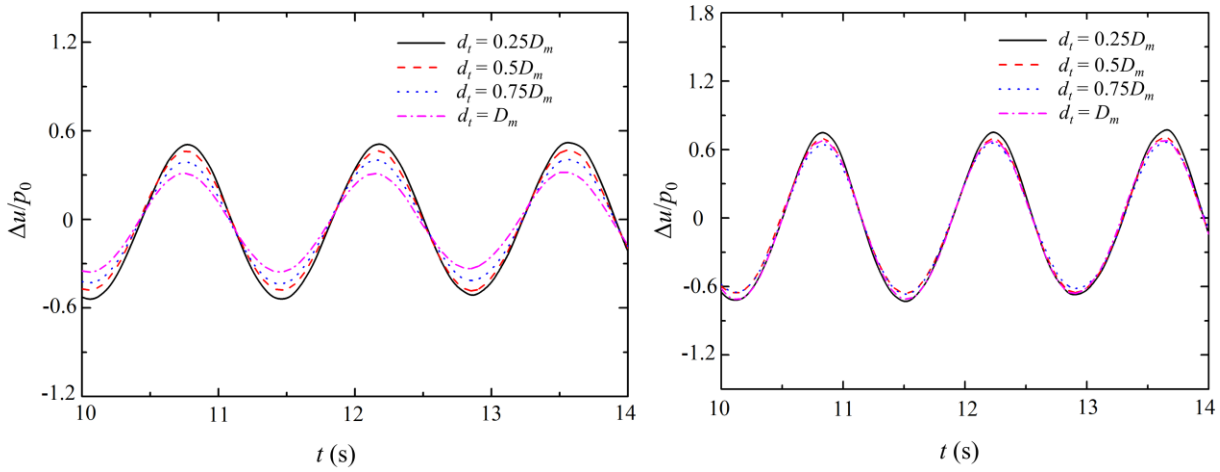

(a) x = 20 m, y = 0.43 m (b) x =20.07 m, y = 0.50 m

734

735 **Fig 13**

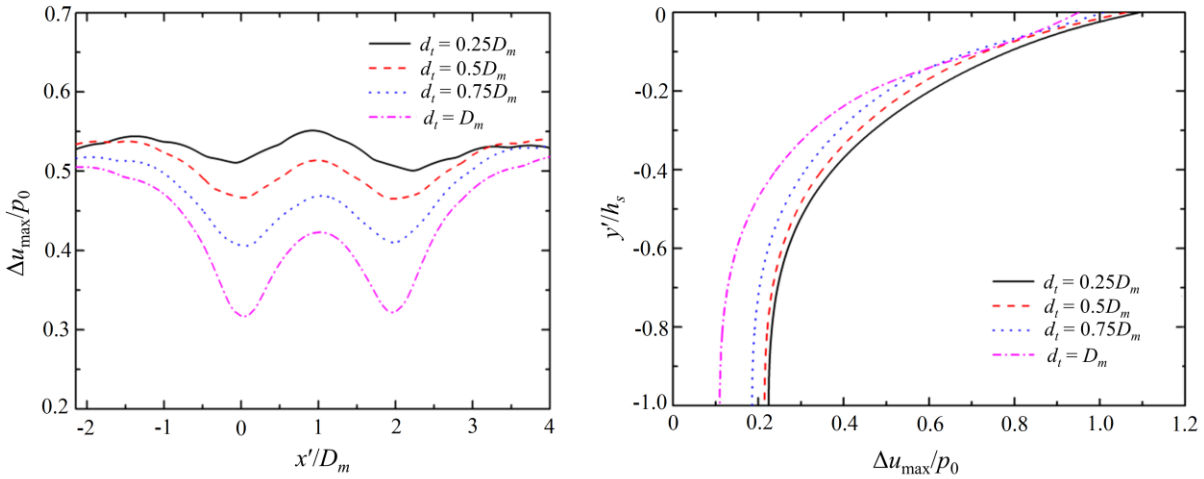

(a) y =0.43 m (b) x =20.07 m

736

737 **Fig 14**

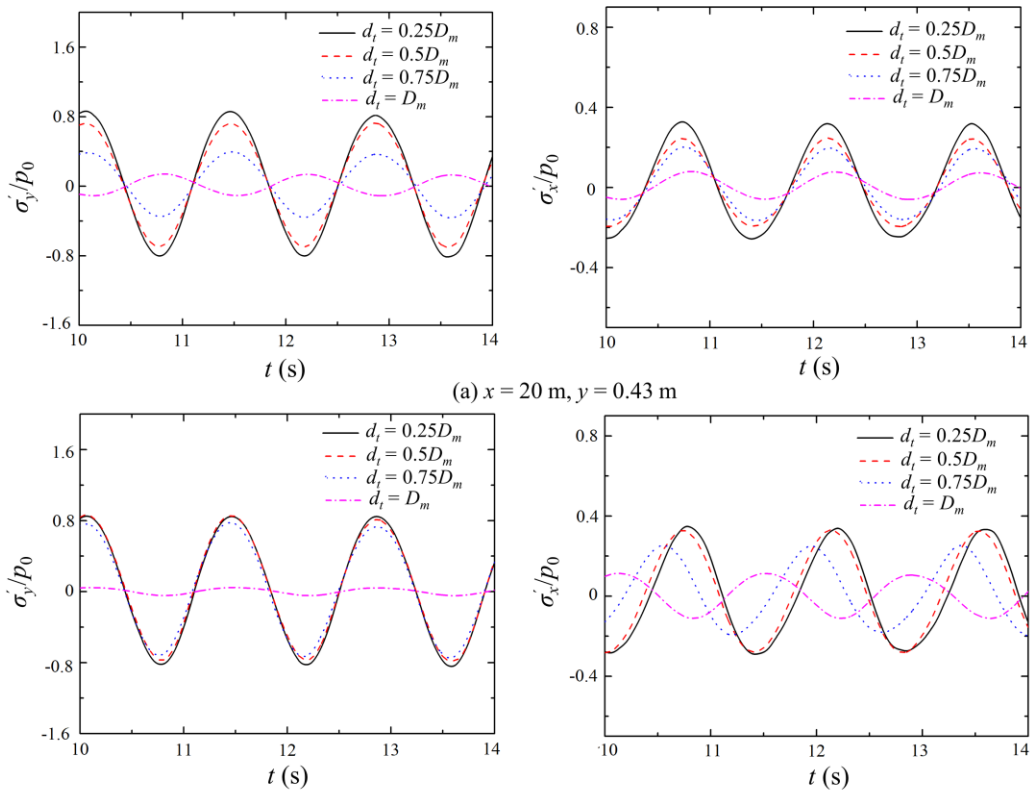

738

739 **Fig 15**

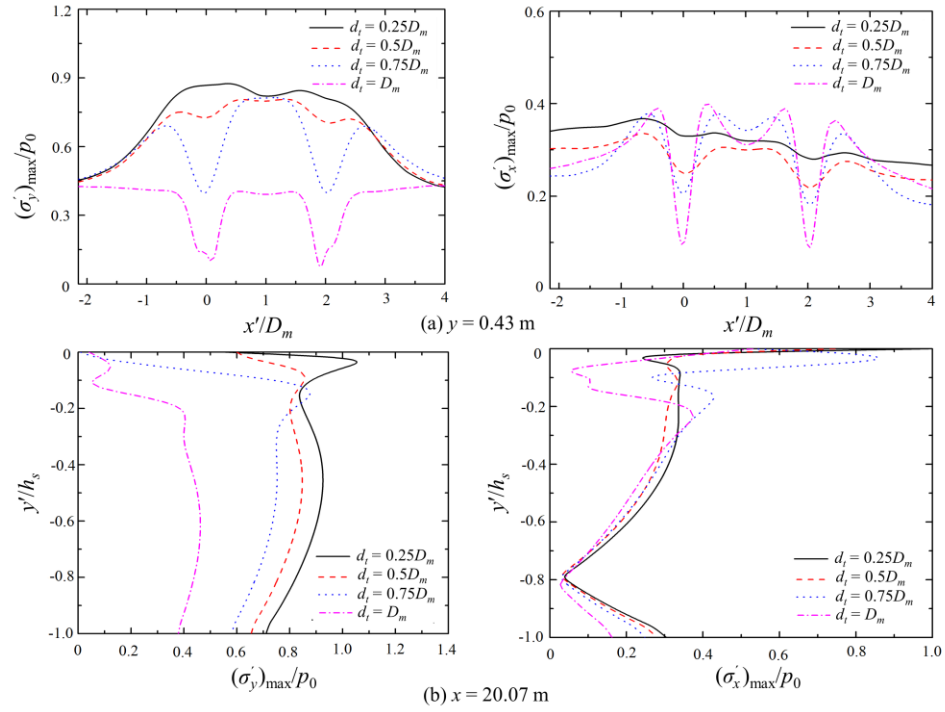

740

741 **Fig 16**

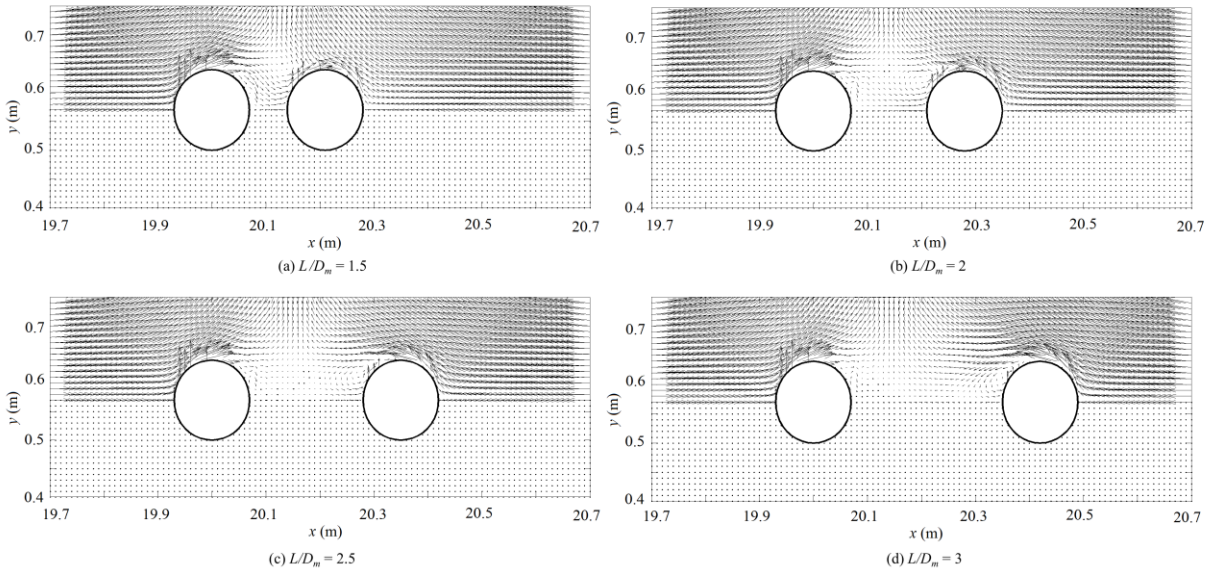

742

743 **Fig 17**

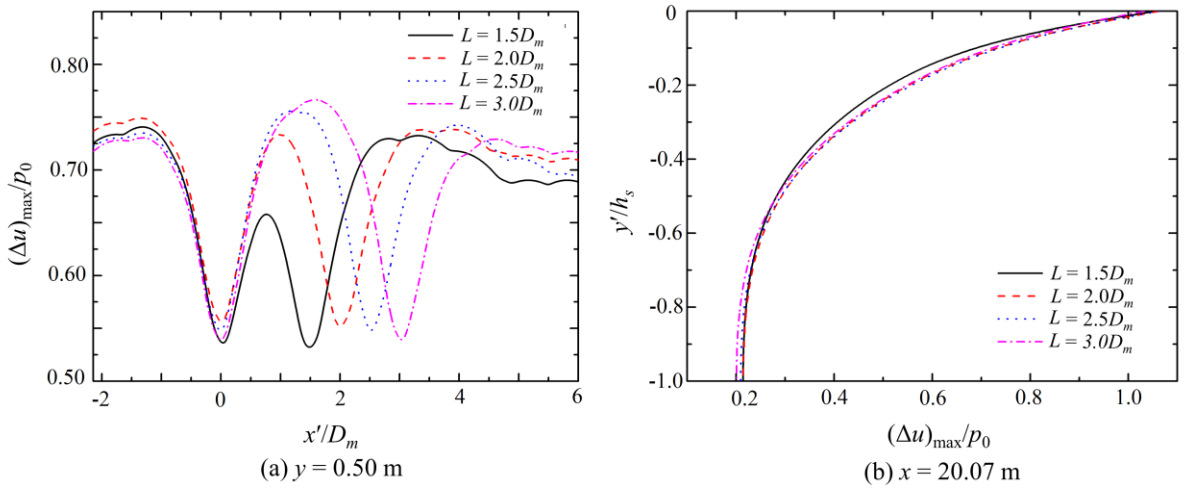

744

745 **Fig 18**

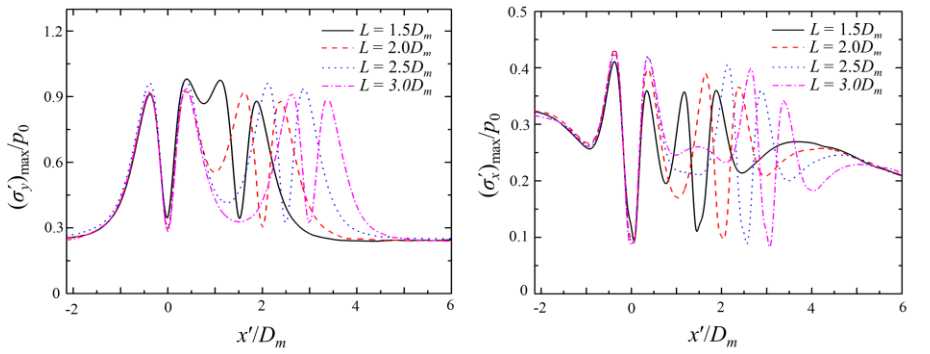

(a) y = 0.50 m

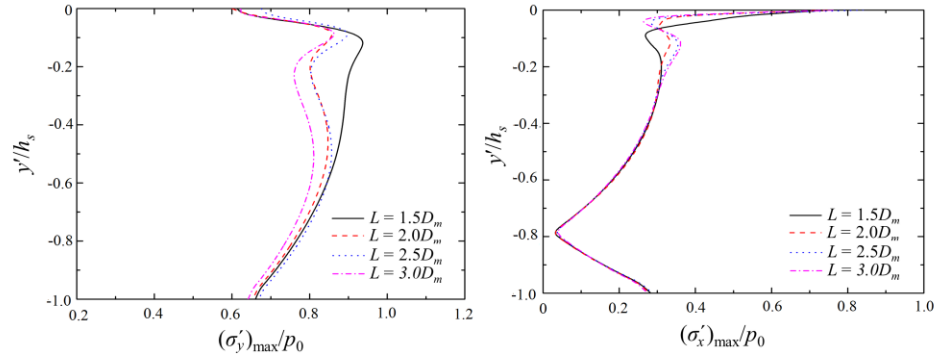

(b) x = 20.07 m

746

747 **Fig 19**